Multiview Positron Attenuation Tomography

Charles C. Watson, *Senior Member, IEEE*

***Abstract*— Positron attenuation tomography (PAT) is a new modality for imaging the linear attenuation coefficients (LACs) of magnetically constrained β^+-ray beams in matter. A complete 3-D LAC image of an object can be made by measuring the positron annihilation rate density within it at a single orientation relative to the beam, and then applying the PAT transformation. The spatial resolution of this image is limited by the resolution of the positron emission tomography (PET), or other, system used to acquire the data as well as the scattering and gyration of the positrons around the magnetic field lines. The finite resolution of the PET system also leads to nonlinear artifacts associated with extended LAC discontinuities parallel to the beam. The mass thickness of an object that can be imaged is limited by the positron beam's range in it. However, due to the directional nature of the imaging process as well as its discrete sampling, PAT images acquired at different view angles may each carry unique information on the object's structure. This paper describes a forward model of PAT image formation and a backpropagation algorithm that, when used together to iteratively combine the data from multiple views, can improve the spatial resolution of PAT LAC images, extend their effective field of view, and reduce artifacts. The technique is demonstrated on measured and simulated data.**

***Index Terms*— Attenuation, beam, positron, tomography.**

I. Introduction

THE ability of a static magnetic field to reduce the transverse range of β^+-rays in matter, thereby potentially improving spatial resolution in positron emission tomography (PET) applications, has been studied extensively since the initial proposal of Iida *et al.* [1]–[4]. Studies at higher field strengths and β^+ energies, and in lower density materials, showed that the distribution of positron annihilations from a point source could be highly asymmetric [5]–[7], and also that this focusing effect could possibly lead to PET image artifacts [8]. The recognition that magnetically constrained positron beams can propagate in air along field lines without appreciable radial divergence for over 50 cm led to the proposal of several practical applications for such beams in an integrated PET/MR (magnetic resonance) medical imaging scanner [9], [10]. It was subsequently discovered that in the 3-T field of a PET/MR, megaelectronvolt (MeV) positron beams attenuated by a factor of 1000 or more while propagating through matter still show minimal divergence. It was additionally recognized that such magnetic collimation of an annihilating beam fully stopped within the view of a PET (or other) annihilation radiation detection system enabled its flux to be measured at all points within an object. This led to the development of the positron attenuation tomography (PAT) technique for 3-D tomographic imaging of the linear attenuation coefficients (LACs) of β^+-ray beams in matter [11], [12], properties that had previously only been accessible through measurement of the transmission of mechanically collimated positron beams through homogeneous slices of materials of varying thickness [13], [14]. This paper describes a new PAT technique using multiple views to improve the accuracy and resolution of such LAC images.

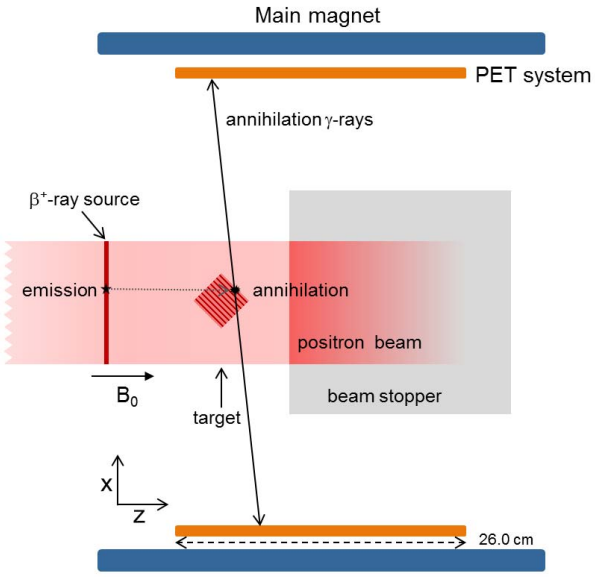

Fig. 1. Schematic of the experimental configuration for PAT on an integrated PET/MRI (not to scale), adapted from [11].

A schematic of a PAT experimental configuration implemented on a Biograph mMR integrated PET/MRI (Siemens) is shown in Fig. 1 [11]. A ^{68}Ga β^+ decay source ($E_{\max} = 1.9$ MeV) is exposed within the field of the 3-T magnet. The emitted positrons follow helical paths around the field lines with gyroradii on the order of 1 mm, and a nondiverging positron beam is formed parallel to $\mathbf{B}_0$ across the PET's field of view (FOV) [10]. Although a PET/MRI is a convenient platform for PAT, the MR imaging capability is not required or used, and other annihilation radiation detection systems besides PET, such as single photon emission computed tomography (SPECT) or a Compton camera, could also be used. Other positron sources could be used as well. Higher energy β^+ decay or accelerator sources could increase the depth of investigation, while lower energy ones could increase sensitivity [11].

Manuscript received September 6, 2017; accepted October 4, 2017. Date of publication October 11, 2017; date of current version November 14, 2017.

The author is with Siemens Medical Solutions USA, Knoxville, TN 37932 USA (e-mail: charles.c.watson@siemens.com).

Color versions of one or more of the figures in this paper are available online at http://ieeexplore.ieee.org.

Digital Object Identifier 10.1109/TNS.2017.2762290

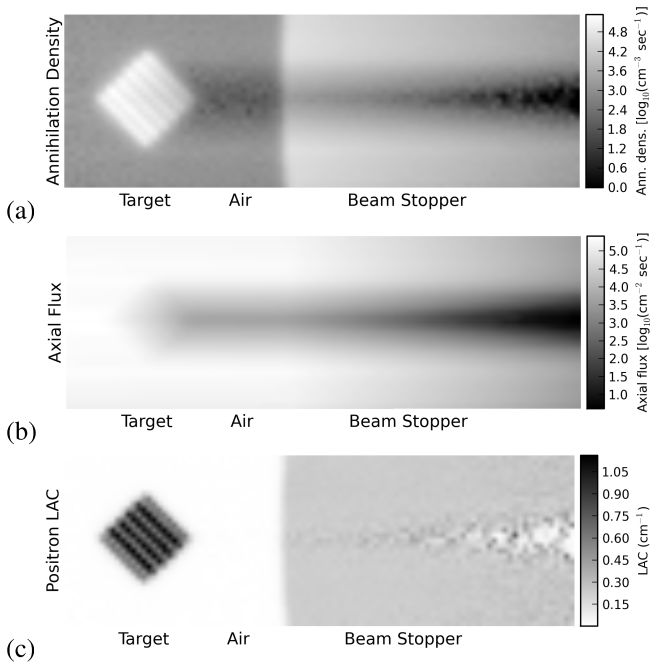

Fig. 2. Generation of a positron LAC image. (a) "PET" image representing the positron annihilation density is acquired. (b) Axial flux image is formed from a cumulative sum of the PET image. (c) PAT LAC image is the ratio of these two. The beam enters from the left. Only part of the beam-stopping block is shown.

Because beam divergence is a negligible effect, the transport equation for the net axial positron flux $\phi_z(\mathbf{r})$ can be written as [11]

$$\frac{\partial \phi_z(\mathbf{r})}{\partial z} = -\mu_z(\mathbf{r})\phi_z(\mathbf{r}) \tag{1}$$

where $\mu_z(\mathbf{r})$ is the LAC of the material at the point $\mathbf{r} = (x, y, z)$. The solution of this equation is

$$\phi_z(\mathbf{r}) = \phi_0(x, y) \exp\left(-\int_0^z \mu_z(\mathbf{r}')dz'\right) \tag{2}$$

where ϕ_0 is the positron flux at some reference point defined as $z = 0$, e.g., as the beam enters the FOV of the PET camera.

The PET component images the annihilation rate along the beam in the air and within any object intersecting it. An example for a 24-mm laminated paper and polymer foam cube in front of a beam-stopping block is shown in Fig. 2(a). Since positrons can only leave the beam through annihilation with an electron, the annihilation rate per unit volume, $\lambda(\mathbf{r})$, quantified in a voxel of the PET image is equal to the product of the flux and the LAC at that point [11]

$$\lambda(\mathbf{r}) = \mu_z(\mathbf{r})\phi_z(\mathbf{r}). \tag{3}$$

It follows from (1) and (3) that, if the beam is fully stopped before axial position z_0 within the PET's FOV, i.e., $\phi_z(x, y, z_0) = 0$, then $\phi_z(\mathbf{r})$ at any point can be estimated from the integral of the annihilation rate downbeam from that point [11]

$$\phi_z(\mathbf{r}) = -\int_z^{z_0} \frac{\partial \phi_z(\mathbf{r}')}{\partial z'}\, dz' = \int_z^{z_0} \lambda(\mathbf{r}')\, dz'. \tag{4}$$

Fig. 2(b) shows an example of such a flux estimate. Once $\phi_z(\mathbf{r})$ is known, $\mu_z(\mathbf{r})$ can be estimated from (3) [11]

$$\mu_z(\mathbf{r}) = \lambda(\mathbf{r}) \Big/ \int_z^{z_0} \lambda(\mathbf{r}')\, dz', \quad z < z_0(x, y). \tag{5}$$

This $\mu_z(\mathbf{r})$ image is shown in Fig. 2(c). It is fully determined by data acquired at a single orientation of the object relative to the beam. Note that this estimate does not require explict knowledge of the flux amplitude ϕ_0.

The accuracy of a single-view LAC image may be limited by several factors. The scattering and gyration of the positrons around the magnetic field lines, and more significantly, the finite spatial resolution of the PET camera, limit the resolution of the LAC image. The discretization of the image relative to the object's structure further degrades resolution and depends on the orientation and position of the object in image space. These effects may reduce the accuracy of the theoretical relation between $\lambda(\mathbf{r})$ and $\phi_z(\mathbf{r})$, which can lead to nonuniform errors in $\mu_z(\mathbf{r})$. Another limitation of single-view imaging is its maximum imaging depth, which is about 0.55 g/cm^2 for a ^{68}Ga positron beam [11]. These factors will be manifested differently for different orientations and positions of the object relative to the beam, and thus, data acquired with different views carry unique information on the object's structure. This can be exploited to improve the accuracy of the LAC map [15].

To this end, this paper describes a multiview reconstruction (MVR) algorithm consisting of a forward model of PAT image formation and a backpropagation algorithm that, when used together to iteratively combine the data from multiple views into a single estimate of the object's structure, can improve the spatial resolution of PAT LAC images, extend their effective FOV, and reduce artifacts. The technique is demonstrated on measured and simulated data. The role of the number and choice of view angles, the influence of the initial estimate, the numbers of iterations, and the PET reconstruction algorithm used are also examined. Some of the results for the laminated foam cube shown here were initially published in [15], and the forward model was originally discussed in [11].

II. Methods

A. Forward Model

The forward model begins from an initial representation of the target LAC image, which may be one of the measured views. To allow for improved resolution information, this target image is represented on a three times finer grid than the measured PET image. The native image pixel size on the mMR is 2.09 mm in transaxial planes and 2.03 mm in the axial direction. This difference will be neglected here, and the PET images are treated as if their pixel size was 2.1 mm isotropically. So the initial $\mu_z(\mathbf{r})$ estimate is upsampled to 0.7-mm pixels. To illustrate the modeling steps more clearly, a synthetic example is discussed here.

An idealized model of a 24-mm laminated cube is shown in Fig. 3(a), consisting of five 4.7-mm-thick layers of polymer foam with paper surfaces. The four interior paper layers are two plies, while the outer two are single ply. The nominal LAC values used were 0.5, 4.5, and 0.008 cm^{-1} for the foam, two plies of paper, and air, respectively. This image is rotated

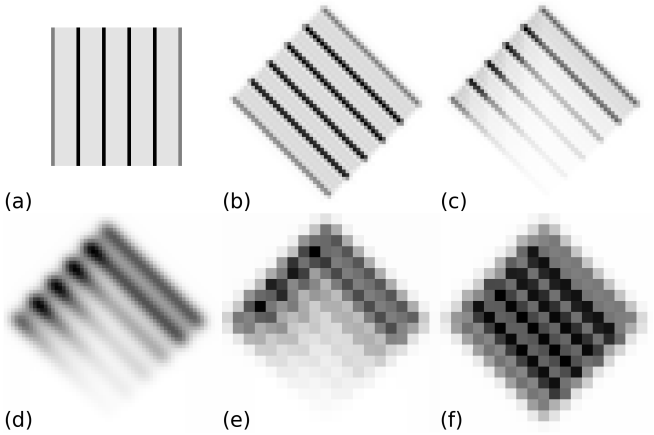

Fig. 3. Six stages of the forward model, shown using nearest neighbor interpolation. (a), (b), and (f) LAC images. (c)–(e) Annihilation intensity distributions. Each image is individually scaled.

and translated to one of the measured image orientations, as necessary. A 45° rotation is shown in Fig. 3(b). The β^+-ray beam is assumed to enter vertically from the top. To approximate the effect of the helical motion and scattering of the positrons, this image is blurred by filtering it with a symmetric 3-D Gaussian kernel having a full width at half maximum (FWHM) of 1 mm. The effect of this blurring is included in Fig. 3(b). An ideal annihilation intensity distribution, shown in Fig. 3(c), is then estimated by substituting (2) (with $\phi_0 = 1$) into (3). If the PAT transform of (5) was applied to this image, the blurred LAC image in Fig. 3(b) would be recovered to within the precision of the numerical integration. To simulate the PET imaging resolution, this annihilation rate distribution is smoothed with a symmetric 3-D Gaussian kernel having an FWHM of 2.5 mm, as shown in Fig. 3(d), and the resulting image is rebinned to 2.1-mm pixels using pixel averaging, as shown in Fig. 3(e). Finally, the PAT transform (5) is applied to this image (including the stopping block) to approximate a measured LAC, as shown in Fig. 3(f). The differences between this image and Fig. 3(b) are due to the resolution smoothing and discretization of the PET image.

This model was validated by comparing it to measurements of a 24-mm laminated foam cube test object constructed similar to the ideal model, as described in the following.

B. Backpropagation

Starting with a measured LAC image at one target orientation, or other initial estimate, upsampled to the finer grid, the forward model is applied to generate estimates of the measured data at all views. The initial image is forced to be nonnegative definite. The update step then proceeds as follows: at each angle, the measured data are divided by the modeled image, and the ratio images are resampled to 0.7-mm pixels. These images are then rotated back to the target image orientation and averaged together. The initial image is multiplied by this mean ratio image to generate an updated image. Symbolically

$$\hat{\mu}_{\text{ref}}^{n+1} = \frac{\hat{\mu}_{\text{ref}}^{n}}{N_a} \sum_{a=1}^{N_a} R_a^- \left[U\left(\frac{\mu_a^{\text{meas}}}{F\left[R_a^+\left(\hat{\mu}_{\text{ref}}^{n}\right)\right]} \right) \right] \tag{6}$$

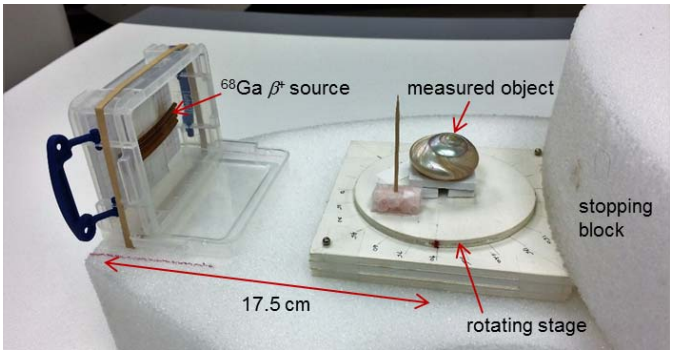

Fig. 4. Apparatus for a multiview PAT measurement.

where $\hat{\mu}_{\text{ref}}$ is the target LAC image view at high resolution, μ_a^{meas} is the measured LAC image at angle a, N_a is the number of measured views used, R_a^+ and R_a^- are, respectively, the forward and backward rotation/translation operators, F is the forward model of the image formation process, and U is an upsampling operator. U estimates the values in the 0.7-mm pixels using a cubic spline interpolation of the 2.1-mm pixel values. This forward-prediction—backpropagation process is iterated, similar to the estimation maximization (EM) update in maximum likelihood estimation maximization PET reconstruction. The procedure can also be applied even if only one angle is measured, in which case it is analogous to "resolution recovery" in PET.

C. Measurements

The experimental apparatus is shown in Fig. 4, mounted on a polymer foam block to minimize attenuation of the annihilation radiation. This structure was placed in the bore of the mMR with the center of the rotation stage 6 cm inside the edge of the PET FOV. The object being measured was placed at the center of the stage and close to the vertical center of the FOV. The β^+-ray source, approximately 11.5 cm outside the PET FOV, consisted of 32.5 MBq of ^{68}Ge/^{68}Ga in four 3-mm-diameter, 70-mm-long lines of bare epoxy resin stacked vertically in a plastic box, forming a beam with a usable imaging height of slightly more than 13 mm vertically, and 70 mm wide horizontally extending into the FOV. The one-sided emission fraction for positrons into the beam for a source of this type is approximately 0.17 [10]. After passing through the object, the beam was stopped within the PET FOV by a polymer foam stopping block whose leading edge was 5.5–6.0 cm behind the center of the rotation stage. This stage was composed of paper covered foam board and was rotated manually between scans. Only 2-D rotations around a vertical axis near the center of the object were made. The vertical wooden stick served as a fiducial marker to assist in registering the images from different views. Acquisition time was 600 s/scan. The annihilation radiation data were reconstructed using the mMR's standard clinical ordinary Poisson-ordered subset estimation maximization (OP-OSEM) algorithm with 3 iterations and 21 subsets, except where otherwise indicated. No corrections for scatter or attenuation of the annihilation radiation were needed or applied, and no postfiltering was used. The PAT transformation (5) was applied

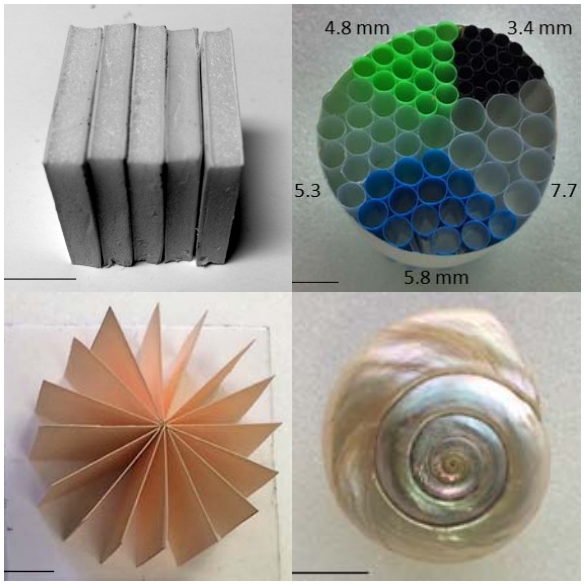

Fig. 5. Measured objects. Clockwise from top left: laminated foam cube, straw array, snail shell, and paper star. The lines at the bottom left are 1 cm.

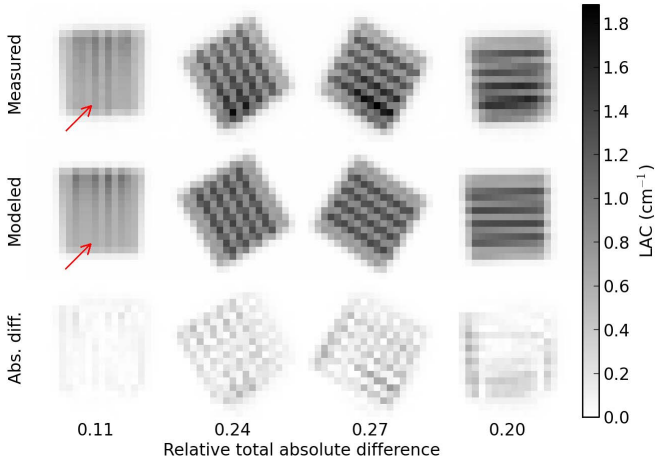

Fig. 6. Measured and modeled PAT LAC images at four-view angles. The third row shows their absolute difference. The numbers are the associated ΔI values, for each angle. The arrows point out the decreasing intensity of the paper laminae along the beam direction.

to these images, together with a beam softening correction discussed in [11]. Experience showed that the beam softening effect, and its correction, had little impact on the modeling of the measured data, and thus was not included in the forward model used for MVR. The PAT measurements and MVRs were 3-D, with an useable vertical thickness of at least six 2.1-mm image planes. In order to reduce noise and small variations due to nonuniformities and imperfect alignment of the nominally vertically uniform objects, the average over their central six coronal slices will be displayed except where otherwise indicated.

The PAT image degradations discussed in Section I are expected to be greater when there are large, discontinuous, variations in LAC. Therefore, objects with high contrast fine structure were used to characterize MVR performance. Measurements were made of the following four objects, as shown in Fig. 5.

1) Laminated Foam Cube: A 24-mm cube consisting of five 4.7-mm-thick layers of polymer foam with paper surfaces as mentioned earlier. This cube was imaged at seven angles relative to the beam: 0°, 15°, 30°, 45°, 58°, 75°, and 92°. Either 10 or 20 update iterations were used in the MVRs. These data were used to verify the forward model, characterize spatial resolution and artifact reduction, and examine the consequences of the choice of initial image and the number of views used in the reconstruction.

2) Straw Array: A 5-cm-diameter array of plastic soda straws with a diameters of 3.4, 4.8, 5.3, 5.8, and 7.7 mm, held together within a paper cylinder 5 cm tall. This array was imaged at 12 angles from 0° to 330° in 30° increments. 20 update iterations were used in the MVRs. These data were used to characterize spatial resolution, examine the impact of the PET reconstruction algorithm, and assess the dependence on the number of views used in the reconstruction.

3) Paper Star: A star shape with 16 fins constructed from heavy weight paper, 5 cm in diameter and 4 cm tall. This structure was imaged at four angular positions differing by increments of 90°. MVRs with 20 and 100 iterations were compared, and a resolution metric was applied to obtain an estimate of the achievable spatial resolution.

4) Snail Shell: This empty shell is 3 × 3.5 cm in the view shown and 1.5 cm thick. It was imaged at 0°, 90°, 180°, and 270° relative to the beam direction, and the data reconstructed with ten iterations. The shell walls are sufficiently thick so that the positron beam is essentially fully absorbed within it at certain locations, leading to defects in the LAC image. The question of interest in this case is how effective multiview imaging is for extending the PAT FOV.

To quantify image differences, a relative total absolute difference metric was used

$$\Delta I = \left(\sum_i \left| I_i - I_i^{\text{ref}} \right| \right) \Big/ \sum_i \left| I_i^{\text{ref}} \right| \tag{7}$$

where I_i is an image with pixel index i and I^{ref} is the image to which it is compared.

III. Results

A. Laminated Cube

Fig. 6 (top row) shows single-view measured LAC images of the laminated cube at angles of 0°, 30°, 58°, and 92° with respect to the beam, which enters vertically from the top here. These images have been averaged over six slices (12.5 mm) of the 3-D image volume. The second row in Fig. 6 shows the results of applying the PAT forward model of Section II-A to the ideal representation of the cube, as shown in Fig. 3, at the measured angles. A quantitative measure of accuracy, the pixelwise absolute difference between the measured and modeled images, is shown in the third row. The associated numbers are the ΔI metric values from (7).

Fig. 7 shows MVR LAC images of both the measured and simulated data from Fig. 6, using all seven of the measured and simulated views, respectively, and ten update iterations per reconstruction. These are also averaged over slices. Each of the four angles shown was used in turn as the target position during the MVR. The pixelwise absolute differences between the measured and modeled images are shown in the third row

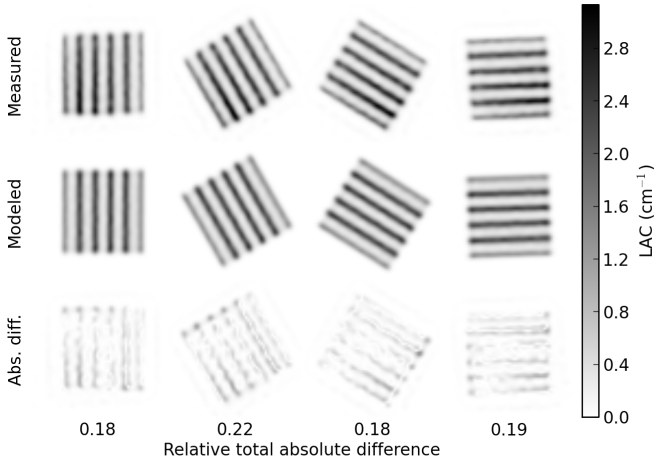

Fig. 7. MVR-PAT LAC images reconstructed from measured and synthetic data at seven view angles, using each of the four shown as the target view. The third row shows the absolute difference of the measured and modeled LACs, similar to Fig. 6, and the numbers are their ΔI values.

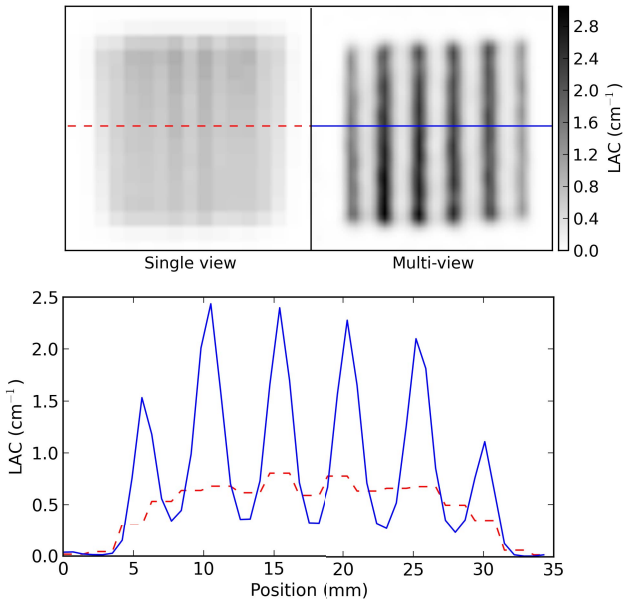

Fig. 8. Top: original measured PAT LAC at 0° versus an MVR image with seven views. Bottom: profiles through these images.

and their associated ΔI values reported, as in Fig. 6. The original measured LAC image at 0° is compared with its MVR estimate in Fig. 8.

The impact of the choice of the initial estimate for MVR is examined in Fig. 9. Results for four MVRs of the laminated cube data using different initial images are shown. In each case, all seven measured views were used, there were 20 iterations, and the target view was the one at 0°. The initial images, shown in the top row, were the measured LAC, a uniform image with value 1, the ideal synthetic image as in Fig. 3, and the ideal image rotated by 90°. The second row shows the MVRs corresponding to these initial assumptions, averaged over slices. As a measure of consistency, the bottom two rows show the results of applying the PAT forward model (Fig. 3) to each of the MVR images to predict the measured data at 0° and 90°.

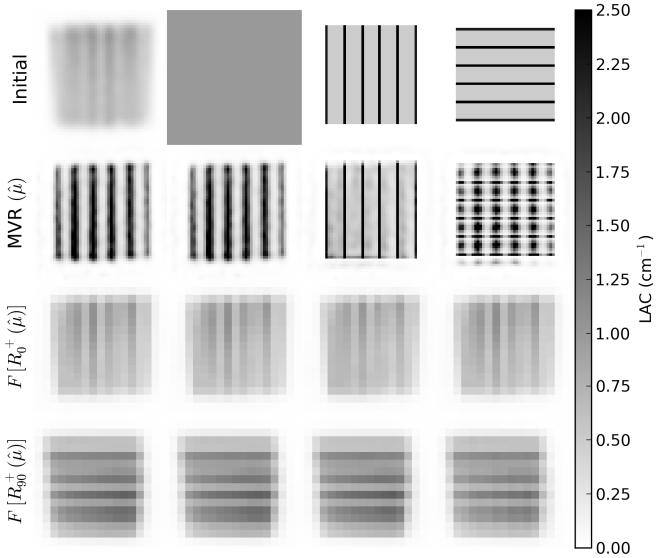

Fig. 9. Top row: four initial images. Second row: corresponding MVRs for the laminated cube data. Bottom two rows: forward model applied to the MVR images at 0° and 90°. The gray-scale window shows 0–22% of maximum.

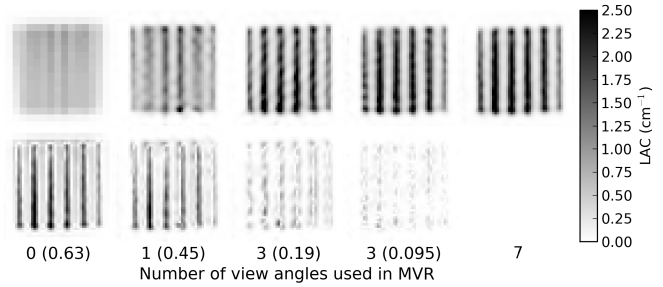

Fig. 10. Top-left to top-right: original PAT; MVR applied to a single view; MVR using three views at 0°, 15°, and 30°; MVR using three views at 0°, 45°, and 92°; MVR using all seven views. The bottom row shows the absolute differences between each image and the seven-view MVR. The numbers in parentheses are the corresponding ΔI values.

The results shown in Fig. 10 characterize the impact of the number and choice of angles in an MVR of the laminated cube data. The leftmost image is the standard single-view PAT at 0°. The second image is the result of applying the MVR algorithm iteratively to this single view. The third and fourth images both used three views for MVR. The third one used the views at 0°, 15°, and 30°, while the fourth used the 0°, 45°, and 92° views. The rightmost image used all seven views available. The second row shows absolute difference images compared with the seven-view MVR and reports their ΔI values. All reconstructions used 20 iterations and the images are averaged over six slices (12.5 mm).

B. Straw Array

Fig. 11 examines the effect of the PET reconstruction algorithm on multiview PAT using the straw array data. Three widely used algorithms provided for clinical use on the mMR were considered: filtered backprojection (FBP), an OP-OSEM algorithm that included modeling of the point spread function (PSF) kernel, and the standard non-PSF OP-OSEM algorithm. No postfiltering or FBP windowing was applied, and the iterative algorithms used 3 iterations

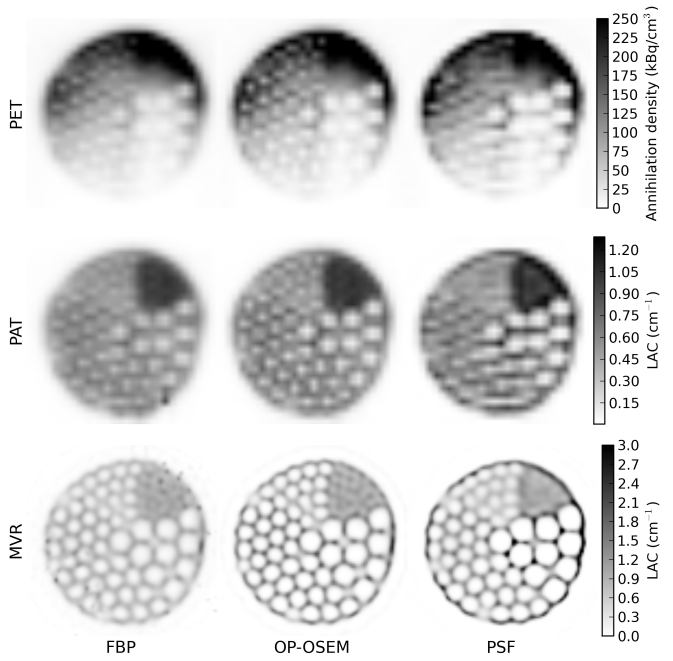

Fig. 11. Three PET reconstructions of the straw array, with corresponding PAT and MVR images. The PAT images are full gray scale; the PET and MVR images have been windowed.

and 21 subsets. The results for the "PET" (i.e., annihilation density) images of the 5-cm straw array are shown in Fig. 11 (top row), with the corresponding single-view PAT LAC images shown in the second row. The bottom row is an MVR using all 12 views, with 20 iterations. These images are displayed with bilinear interpolation and represent an average over six slices.

The 5-cm straw array also provides another opportunity to examine MVR image quality versus number of views. These data were reconstructed using one (0°), two (0° and 180°), three (0°, 120°, and 240°), four (0°, 90°, 180°, and 270°), six (0°, 60°, 120°, 180°, 240°, and 300°), and all twelve measured views. The target view was 0° in all cases, and 20 iterations were used. The results are shown in Fig. 12(a), averaged over six slices. These may be compared with the OP-OSEM PAT image in Fig. 11. Fig. 12(b) shows the absolute differences between each image in Fig. 12(a) and the 12-view MVR. The numbers in parentheses are their ΔI values.

C. Paper Star

A third resolution evaluation was made using the paper star phantom. A single-view PAT image of this phantom is shown in Fig. 13(a), averaged over the six central slices in the beam. The MVR of the four measured views is shown in Fig. 13(c) at 20 and 100 iterations. The average over slices is compared with a central slice image. A close-up of the slice-averaged image at 20 iterations is shown in Fig. 13(b). The red circle is centered on the star and has a radius of 9.8 mm. Image profiles around this circle are plotted in Fig. 13(d) for both the original PAT image in Fig. 13(a) and the MVR image in Fig. 13(b).

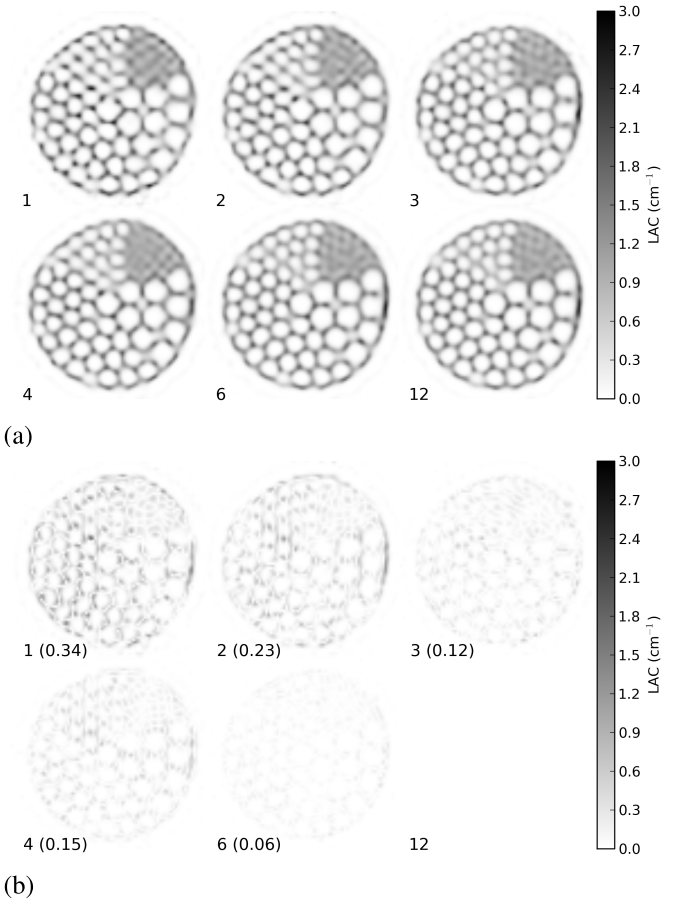

Fig. 12. (a) MVRs of the straw array, with varying numbers of views as indicated. The gray scale is windowed and the image pixels are bilinearly interpolated. (b) Absolute differences between each image in (a) and the 12-view MVR. The numbers in parentheses are the corresponding ΔI values.

D. Snail Shell

The set of four PAT LAC images acquired of the snail shell are shown in Fig. 14(a). These are central coronal slices from the image volume. The beam enters vertically from the top. Fig. 14(b) shows central coronal and transaxial slices through a composite of the four image volumes obtained by interpolating the four measured images in Fig. 14(a) to 0.7-mm pixels, rotating them to 0°, and averaging. This image was then used as the initial image for an MVR of the four measured views with ten iterations. Central coronal and transaxial slices of the resulting MVR are shown in Fig. 14(c). The transaxial view is through the shell at its thickest point and spans the positron beam, which is tapering off at the bottom.

IV. Discussion

A. Laminated Cube

The comparison between the measured and modeled images in Fig. 6 suggests the accuracy with which the PAT imaging process can be modeled. Some of the variations seen between the measurements and model may have to do with the precise positioning of the cube relative to the image pixels, and to small irregularities in the physical object. It can be seen that when the cube's paper laminae are parallel to the beam, they show much less contrast compared with

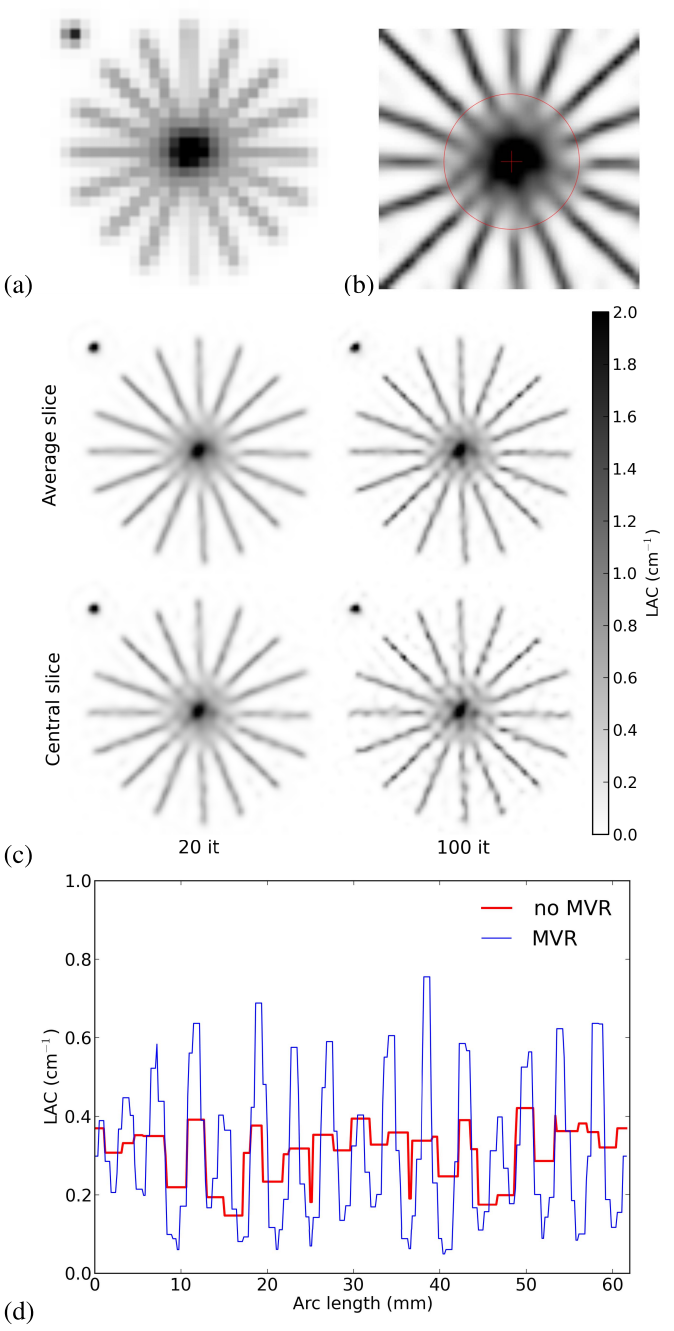

Fig. 13. Paper star phantom. (a) Original PAT LAC image at 0°. (b) Central portion of the MVR's average slice at 20 iterations. (c) MVR PAT images with 20 and 100 iterations. (d) Profiles around the circle shown in (b), for the original PAT (no MVR) and MVR images.

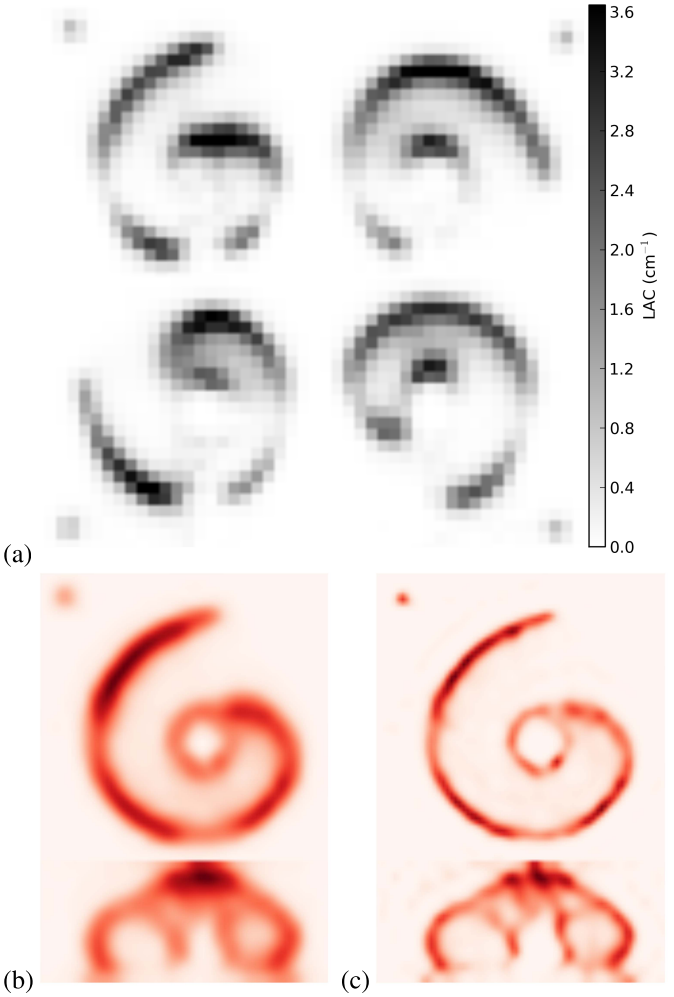

Fig. 14. Snail shell. (a) Central coronal slices of the original PAT LAC images. (b) Central coronal and transaxial slices of the average LAC. (c) Corresponding slices of the MVR. For (b) and (c), the color scale is individually normalized for each slice.

other views, and appear to taper off from top to bottom (arrows). This effect can be understood as a consequence of the PET camera's finite resolution: transverse smoothing of the annihilation density essentially averages together two exponential attenuation processes as in (2). Assuming the flux entering the cube is similar to the foam and paper regions, the annihilation density in the foam will exceed that in this paper for $\Delta z > \ln(\mu_z^p/\mu_z^f)/(\mu_z^p - \mu_z^f) \geq 5.5$ mm, where $\mu_z^p = 4.5$ cm^{-1} and $\mu_z^f = 0.5$ cm^{-1} are the effective paper (after positron blurring) and foam LACs, respectively. At axial length scales greater than this the transverse point spread in the PET's response, being much wider than the paper thickness, will cause the observed $\lambda(\mathbf{r})$ to be more and more similar to pure foam, causing the apparent tapering off of the laminae, as indicated by the arrows in Fig. 6. This is a nonlinear process distinct from the typical spatial blurring in PET. A goal of multiview imaging is to reduce such artifacts.

The similarity between the measured and simulated MVR results in Fig. 7 further supports the adequacy of the forward model. These MVR images are apparently more accurate, and much less dependent on orientation, than the single-view images. The resolution is greatly improved, particularly for the 0° view, as can be seen in Fig. 8. While the laminae are barely visible in the original image, they are well defined in the MVR image. Recall that the pitch of these laminae is 4.7 mm, which is similar to the minimum nominal PET resolution of this machine (4.2-mm FWHM). It thus appears that MVR can substantially exceed the intrinsic PET resolution capability.

It is not too surprising that MVR produces essentially the same image (aside from rotation) when any one of the measured views is used as the starting point, since in this

case all reconstructions use exactly the same data. However, significant variations may arise when the initial estimate is not one of the measured views, as shown in Fig. 9. While there is essentially no difference between using the measured view or a uniform image as the initial estimate, when the initial image is a high-resolution representation of the true object (third column), MVR largely preserves this structure. On the other hand, when the initial estimate is very inconsistent with the measured data, as in the right column, MVR cannot fully resolve this error. The bottom two rows of Fig. 9 help explain why this happens. These predictions are very similar regardless of the MVR image on which they are based. This suggests that the forward model effectively has a null space containing the differences between the MVR images shown. Equivalently, all four MVR images are (approximately) stationary points of the iterative algorithm. These results further suggest that while it is important not to initialize the reconstruction with a highly inaccurate assumption (as in the fourth column), it might be possible to advantageously incorporate *a priori* knowledge of the object's structure (as in the third column).

The results in Fig. 10 show that while the single-view processing does recover some resolution, the three-view MVRs are significantly better, with the one using 0°, 45°m and 92° slightly preferred. The full seven-view MVR has noticeably less error in structure. The quantitative relative total absolute difference metric confirms the visual impression of image quality.

B. Straw Array

Fig. 11 shows that the choice of the PET reconstruction algorithm has a significant impact on MVR PAT image quality. The FBP reconstruction produces somewhat lower resolution images than OP-OSEM with some apparent noise artifacts. The PSF images show a noticeable loss of resolution in the 3.4- and 4.8-mm straw segments compared with the OP-OSEM reconstruction and exhibit edge overshoot artifacts in the 7.7-mm segment and around the outer boundary. This is a consequence of the inaccurate shape of the particular kernel used in this algorithm [9], [16]. All other results reported in this paper used non-PSF OP-OSEM for reconstruction.

The single-view reconstruction of the straw array data in Fig. 12 improves resolution, but leaves significant residual distortion. The use of multiple views further improves the accuracy of the image. Most of the benefit is achieved with three or four angles. There is only a 6% relative absolute difference between the MVRs with 6 and 12 views. Although each new view may bring additional information on the object, it also potentially contains errors in the accuracy of the angle and center of rotation of the view. This could explain why the 3-view MVR has slightly less error relative to the 12-view reconstruction than the 4-view MVR does, for example. These results suggest that MVR PAT resolution using ^{68}Ga positrons on the 3 T mMR is below 4.8 mm, the diameter of the straws in the smallest clearly resolved segment. This is consistent with the results for the laminated cube experiment (Fig. 8), and far better than the resolution observed in the corresponding PET image (Fig. 11).

C. Paper Star

The convergence (or nonconvergence) characteristics of the MVR algorithm have not yet been explored, but the 100 iteration images in Fig. 13(c) show a buildup of some numerical errors that, particularly in the single slice image, appear to be associated with the pixelation of the PAT images. This may be due to inaccuracies in the forward model. The spatial resolution of the slice-averaged image at 20 iterations appears to be nearly uniform from the edge toward the center of the phantom until a radius of about 9.8 mm is reached, as shown by the circle in the close-up in Fig. 13(b). At smaller radii, it becomes difficult to resolve all the fins. The profile plots in Fig. 13(d) give an idea of the resolution improvement that can be attained with MVR. The average fin separation around this circle, 3.85 mm, is another estimate of MVR PAT's resolving power and is consistent with the previous two.

D. Snail Shell

Although there is good reason to believe that the LAC of the snail's shell is more or less uniform along its wall, there are significant deficits in the LAC images in Fig. 14(a). This happens because the PAT transform fails where the beam is nearly or completely absorbed in the shell, and the PET image values are dominated by background and noise. The sources of this background may include the intrinsic bias of the EM algorithm at low counts, bias in the randoms correction, or possibly scattering of the annihilation radiation. It is typically several orders of magnitude below the maximum intensity values in an image, and difficult to quantitatively predict. It impacts the LAC estimate primarily because it invalidates (4) and causes the flux to be overestimated, thereby reducing the apparent LAC calculated in (5). A similar effect can be seen in Fig. 2(c) (right) as the beam nears the end of its range in the stopping block.

It is not possible to recover these defect regions from a single view. However, as the shell is rotated, these deficits occur in different regions, so that a combination of views can provide more complete information on the structure. Experience shows that it is not adequate to use one of the measured views as the initial image for the MVR in cases like this. Because the forward model cannot accurately predict these regions of signal loss, they tend to propagate and lead to artifacts in the MVR. Instead, a better choice is to use the average of the measured images (rotated to the same angle) as an initial image, as is shown in Fig. 14(b). Although the shell wall is now complete in the coronal slice of the resulting MVR image shown in Fig. 14(c), it is still not uniform, with low values of μ_z where voids occur in one or more of the individual LAC images. The voids in one view are effectively just being averaged together with the measured regions in others, reducing the estimated values there. To overcome this problem, the PAT forward model and backpropagation update operator would need to be modified to explicitly account for the background and noise in the PET images when they become dominant as the beam approaches full absorption, and exclude contributions from these regions.

E. Potential Applications

Multiview PAT is a useful tool for understanding the physics of magnetically constrained positron beams in matter and could be a practical alternative for measuring positron (and electron) attenuation in tissues and materials for dosimetry and radiation shielding purposes. In combination with X-ray computed tomography (CT), which measures photon Compton and photoelectric cross sections, PAT could add a new positron annihilation dimension to materials characterization, particularly for lower density materials where it has a large sensitivity advantage over CT [10]. This high sensitivity suggests possible applications in visualizing gas and fluid flow through lightweight porous materials, for example [11]. The inherent beam softening effect in PAT can in principle provide a means for attenuation correction in beta emission imaging [11], [17], because the amount of beam softening, which can be quantified with PAT, is systematically related to the degree of attenuation experienced by the positrons. It seems likely that multiview PAT will find other applications in materials, radiation, and biological sciences as well.

F. Limitations and Future Work

The results presented in this initial paper on multiview PAT are necessarily limited in scope. While it is clear that the technique can quantitatively improve resolution and reduce artifacts in positron LAC images, many questions remain. The number and choice of view angles can undoubtedly be optimized, but may depend on the structure of the object. Polar as well as azimuthal view rotations need to be considered. Small translations of the object between scans could possibly be useful as well. The forward model and backpropagation components of the MVR algorithm could be refined, and its convergence characteristics need to be established. The choice of the initial image clearly has an impact that needs to be evaluated further. The use of *a priori* information or data from other modalities, such as X-ray CT, could bring significant benefits. Improvements that might be achieved by using higher energy positron beams and higher magnetic field strengths would be very interesting to investigate, as would the benefit of using a higher resolution system for imaging the annihilation radiation, similar to a dedicated small animal PET. Finally, the possible benefit of multiview PAT for imaging low-contrast objects also remains to be explored.

V. Conclusion

Multiview PAT can improve the resolution of single-view PAT, reduce artifacts, and extend its imaging range. Spatial resolution superior to the PET camera used for the measurements can be achieved. The number of views and their distribution affect the resulting image, and thus can be optimized, but even a small number of views widely spaced in angle are beneficial. The initial image used for the reconstruction plays an important role, as does the choice of the PET reconstruction algorithm. The convergence properties of the MVR algorithm proposed here are not yet fully characterized, but 10–20 iterations gives reasonable results in all cases examined so far; additional iterations seem to have little benefit. The accuracy of the forward model presented here is good, but could undoubtedly be improved. An algorithmic refinement is needed to deal more robustly with the signal loss at the end of the positron beam's range.

References

[1] H. Iida, I. Kanno, S. Miura, M. Murakami, K. Takahashi, and K. Uemura, "A simulation study of a method to reduce positron annihilation spread distributions using a strong magnetic field in positron emission tomography," *IEEE Trans. Nucl. Sci.*, vol. NS-33, no. 1, pp. 597–600, Feb. 1986. [Online]. Available: http://dx.doi.org/10.1109/TNS.1986.4337173

[2] B. E. Hammer, N. L. Christensen, and B. G. Heil, "Use of a magnetic field to increase the spatial resolution of positron emission tomography," *Med. Phys.*, vol. 21, no. 12, pp. 1917–1920, Dec. 1994. [Online]. Available: http://dx.doi.org/10.1118/1.597178

[3] R. R. Raylman, B. E. Hammer, and N. L. Christensen, "Combined MRI-PET scanner: A Monte Carlo evaluation of the improvements in PET resolution due to the effects of a static homogeneous magnetic field," *IEEE Trans. Nucl. Sci.*, vol. 43, no. 4, pp. 2406–2412, Aug. 1996. [Online]. Available: http://dx.doi.org/10.1109/23.531789

[4] A. Wirrwar, H. Vosberg, H. Herzog, H. Halling, S. Weber, and H.-W. Müller-Gärtner, "4.5 tesla magnetic field reduces range of high-energy positrons-potential implications for positron emission tomography," *IEEE Trans. Nuc. Sci.*, vol. 44, no. 2, pp. 184–189, Apr. 1997. [Online]. Available: http://dx.doi.org/10.1109/23.568801

[5] D. Burdette *et al.*, "A study of the effects of strong magnetic fields on the image resolution of PET scanners," in *Proc. IEEE Nucl. Sci. Symp. Conf. Rec.*, Oct./Nov. 2007, pp. 3383–3389. [Online]. Available: http://dx.doi.org/10.1109/NSSMIC.2007.4436857

[6] H. Herzog *et al.*, "Influence from high and ultra-high magnetic field on positron range measured with a 9.4TMR-BrainPET," in *Proc. IEEE Nucl. Sci. Symp. Conf. Rec.*, Oct./Nov. 2010, pp. 3410–3413.[Online]. Available: http://dx.doi.org/10.1109/NSSMIC.2010.5874439

[7] N. J. Shah *et al.*, "Effects of magnetic fields of up to 9.4 T on resolution and contrast of PET images as measured with an MR-BrainPET," *PLoS ONE*, vol. 9, no. 4, p. e95250, Apr. 2014. [Online]. Available: http://dx.doi.org/10.1371/journal.pone.0095250

[8] A. Kolb *et al.*, "Shine-through in PET/MRI: Effects of the magnetic field on positron range and subsequent image artifacts," *J. Nucl. Med.*, vol. 56, no. 6, pp. 951–954, Jun. 2015. [Online]. Available: http://dx.doi.org/10.2967/jnumed.114.147637

[9] C. C. Watson, "Measurement of the physical PSF for an integrated PET/MR using targeted positron beams," in *Proc. IEEE Nucl. Sci. Symp. Conf. Rec.*, Oct./Nov. 2012, pp. 2089–2095. [Online]. Available: https://doi.org/10.1109/NSSMIC.2012.6551480

[10] C. C. Watson, L. Eriksson, and A. Kolb, "Physics and applications of positron beams in an integrated PET/MR," *Phys. Med. Biol.*, vol. 58, no. 3, pp. L1–L12, Feb. 2013. [Online]. Available: http://dx.doi.org/10.1088/0031-9155/58/3/L1

[11] C. C. Watson, "Imaging the attenuation coefficients of magnetically constrained positron beams in matter," *Nucl. Instrum. Methods Phys. Res. B, Beam Interact. Mater. At.*, vol. 383, pp. 234–244, Sep. 2016. [Online]. Available: http://dx.doi.org/10.1016/j.nimb.2016.07.008

[12] C. C. Watson, "Positron attenuation tomography," U.S. Patent 9 651 687, May 16, 2017. [Online]. Available: http://patft.uspto.gov

[13] S. R. Thontadarya and N. Umakantha, "Comparison of mass absorption coefficients of positive and negative beta particles in aluminum and tin," *Phys. Rev. B, Condens. Matter*, vol. 4, no. 5, pp. 1632–1634, Sep. 1971. [Online]. Available: http://dx.doi.org/10.1103/PhysRevB.4.1632

[14] J. R. Patrick and A. S. Rupaal, "Transmission of low energy positrons and electrons through thin metallic foils," *Phys. Lett. A*, vol. 35, no. 4, pp. 235–236, Jun. 1971. [Online]. Available: http://dx.doi.org/10.1016/0375-9601(71)90357-4

[15] C. C. Watson, "Improved resolution in positron attenuation tomography using multiple views," in *Proc. Nucl. Sci. Symp., Med. Imag. Conf. Room-Temperature Semiconductor Detect. Workshop (NSS/MIC/RTSD)*, Oct. 2016, paper M20-2, doi: 10.1109/NSSMIC.2016.8069628.

[16] A. Rahmim, J. Qi, and V. Sossi, "Resolution modeling in PET imaging: Theory, practice, benefits, and pitfalls," *Med. Phys.*, vol. 40, no. 6Part1, p. 064301, Jun. 2013. [Online]. Available: http://dx.doi.org/10.1118/1.4800806

[17] C. C. Watson, "Magnetic lens technique for improving the resolution of beta emission imaging," U.S. Patent Application, Jul. 5, 2017.